Characterization of the convoluted 3D intermetallic phases in a recycled Al alloy by synchrotron X-ray tomography and machine learning

Zhenhao Li[1], Ling Qin[3], Baisong Guo[1], Junpin Yuan[2], Zhiguo Zhang[1*], Wei Li[1], Jiawei Mi[3*]

[1]Institute of Advanced Wear Resistant and Functional Materials, Jinan University, Guangzhou 510632, China

[2]Jewelry Institute, Guangzhou Panyu Polytechnic, Guangzhou 511487, China

[3]Department of Engineering, University of Hull, East Yorkshire HU6 7RX, UK

ABSTRACT Fe-rich intermetallic phases in recycled Al alloys often exhibit complex and 3D convoluted structures and morphologies. They are the common detrimental intermetallic phases to the mechanical properties of recycled Al alloys. In this study, we used synchrotron X-ray tomography to study the true 3D morphologies of the Fe-rich phases, Al_2Cu phases and casting defects in an as-cast Al-5Cu-1.5Fe-1Si alloy. Machine learning based image processing approach was used to recognize and segment the different phases in the 3D tomography image stacks. In the studied condition, the β-$Al_9Fe_2Si_2$ and ω-Al_7Cu_2 are found to be the main Fe-rich intermetallic phases. The β-$Al_9Fe_2Si_2$ phases exhibit a spatially connected 3D network structure and morphology which in turn control the 3D spatial distribution of the Al_2Cu phases and the shrinkage cavities. The Al_3Fe phases formed at the early stage of solidification affects to a large extent the structure and morphology of the subsequently formed Fe-rich intermetallic phases. The machine learning method has been demonstrated as a powerful tool for processing big datasets in multidimensional imaging-based materials characterization work.

Keywords: Recycled Al alloy, solidification, synchrotron X-ray tomography, machine learning, Fe-rich intermetallic phases.

Corresponding authors Z. Zhang zhigzhang@jnu.edu.cn; J. Mi J.Mi@hull.ac.uk

1. Introduction

Aluminium (Al) and its alloys have been widely used in transportation, aerospace, construction, packaging and electrical industry due to their high strength-to-weight ratio, excellent corrosion resistance, good electrical conductivity and fully recyclable nature [1-2]. Maximising the uses of recycled Al alloys and the relevant products is the most economical and effective strategy in developing a sustainable and resource-efficient operation in global Al industry for reducing CO_2 emission in primary Al production in the future circular economy [3]. However, in the repeated Al scrap sorting, remelting and remanufacturing processes, detrimental impurity elements are gradually accumulated, resulting in degraded mechanical properties for the recycled Al alloys. Fe, in particular, is the most detrimental element for almost all Al alloys because it has a very low solid solubility (0.05 wt.%) in Al matrix at room temperature, forming different types of Fe-rich intermetallic compounds depending on the actual alloy compositions [4-5]. The most common Fe-rich phases in recycled Al alloys containing Fe and Si are α-Fe phase (Al_8Fe_2Si) and β-Fe phase ($Al_9Fe_2Si_2$), called α-Fe and β-Fe hereafter. The β-Fe is a brittle phase with complex 3D network structures and is predominantly the site for initiating crack during mechanical loading [6]. Therefore, it is crucial to understand the nucleation and morphology evolution of the Fe-rich intermetallic phases and then develop cost-effectively processing strategy to either remove the excessive Fe from the recycled Al alloys, or to control or to alter the Fe-rich intermetallic phases into a less detrimental shape and morphology.

In the past 20 years or so, synchrotron X-ray imaging and tomography techniques have been increasingly used to study in real-time the dynamic microstructure evolution of metallic alloys in the solidification processes [7-13], for example, the growth dynamics and fragmentation of dendrites [8] and intermetallic phases [9-10] during

ultrasound melt processing, which provides direct evidence and enormous real-time datasets for understanding precisely the phase formation and 3D structure evolution in the dynamic solidification processes, for example, the complex 3D structure of Fe-rich intermetallic phases [11-12] and metal carbides in Ni superalloy [13]. However, due to the enormous amount of data obtained in a typical X-ray high speed imaging and/or tomography experiment (a few to a few tens of TB data is common in a single experiment), it is a challenging task to achieve high fidelity data segmentation and accurate quantitative analysis in an efficient and effective way. The reason is that the solidification microstructures often consist of multiple phases with different X-ray contrasts entangled and convoluted in 3D space. There is no single imaging processing strategy that works well for all phases. Phase recognition, identification and segmentation are often carried out semi-automatically or sometimes manually by experienced materials scientists, which is laborious, time-consuming and sometimes inaccurate.

Machine learning methodologies and efficient data analysis algorithms have been increasingly adopted for analyzing and processing big-data, especially in the fields of image recognition, process optimization, component dimensional accuracy analysis, manufacturing defect identification and material property prediction [14-17]. For example, the machine learning approaches applied to image segmentation, feature extraction, and classification of the CT scanned images from a human being have greatly aided the diagnosis of illness [18]. However, applying machine learning methods in processing synchrotron X-ray 3D tomographic datasets of solidified microstructures is still a challenging task because (1) for most industrial alloys, the solidification phases have complex structures entangled and convoluted in 3D space; (2) the X-ray contrasts between different phases due to absorption (although maybe

3

enhanced by phase contrast effects) are not higher enough for a straightforward identification and segmentation.

In this study, we used a machine learning based image processing plugin in Fiji software (Trainable Weka Segmentation [19]) to analyze the synchrotron X-ray tomography datasets of a recycled Al-5Cu-1.5Fe-1Si alloy and quantify the different phases in 3D space. The research indicates that machine learning based approach can significantly improve the quality of the phase segmentation and identification as well as the true 3D morphologies of the phases. This work illustrates an exemplary case of using the advanced scientific tools and methodology, i. e. synchrotron X-ray tomography, supercomputing plus machine leaning to quantify accurately and efficiently the complex 3D phases in recycled Al alloys which is essential for further implementing optimal phase control strategy in the solidification processes.

2. Experimental methods

The alloy used was Al-5Cu-1.5Fe-1Si (weight percentage) and 300 g of such alloy was made by melting pure Al (99.99%), pure Cu (99.99%), pure Fe (99.99%) and high-purity Al-20%Si alloy ingots together. Firstly, pure Al and Al-20%Si alloy ingots were melted at 800 °C in a boron nitride coated alumina crucible inside an electrical resistance furnace. Then, small pieces of pure Fe and pure Cu bars were added into the melt and held at 800 °C for 2 hours to melt the Fe and Cu completely. Frequent stirring of the melt was carried out during the melting to avoid the sediment of the Fe and Cu elements. A bespoke counter-gravity casting apparatus [20] was used to draw the molten alloy to flow uphill into a 10 mm diameter and 80 mm long quartz tube and solidified there to form the as-cast rods. The rods were then removed from the quartz tubes and machined into 2 mm diameter rods for tomography scans.

Phases of the as-cast Al-5Cu-1.5Fe-1Si alloy samples were analyzed by X-ray diffraction (XRD, Rigaku Ultima IV), scanning electron microscope (SEM, Phenom XL) equipped with an X-ray energy dispersive spectroscopy (EDS).

The synchrotron X-ray tomography experiments were carried out at the ID19 beamline of the European Synchrotron Radiation Facility (ESRF) using the same setup and parameters as detailed in Table 1 of [21]. Pink X-ray beam of 26 KeV and a PCO. DIMAX camera were used to record the X-ray projections while the samples were rotated over 180 degrees. 1000 projections were acquired in each rotation with 2 ms exposure time for each projection. A 10× optical lens was used to magnify the projections, achieved an effective pixel size of 1.1 μm/pixel in a field of view (FOV) of 1008×1008 pixels. 3D tomographic reconstruction was made using the ESRF reconstruction algorithm with phase retrieval functionality [22].

The open-source Fiji software was used to filter the reconstructed tomography image stacks (including denoise, gray balance, normalization, etc.). The machine learning based image processing tool is the Trainable Weka Segmentation plugin installed in Fiji software [19]. It can enhance solidification phase recognition and segmentation for each individual 2D slice of the tomography image stack. Then, the segmented image stacks were loaded into the Avizo 9.4 software (FEI, France) for further visualization and analysis. For each phase, the 3D equivalent diameter and the 3D thickness were used to quantify the morphology characteristics of each phase. The 3D equivalent diameter is defined as $D = 2 * (\frac{3V}{4\pi})^{\frac{1}{3}}$, where V is the volume of a single-phase or a cluster. 3D thickness is defined as the largest segment that touches the object by its end points and lying in a plane orthogonal to the maximum 3D Feret diameter and orthogonal to the breadth 3D diameter. 3D Feret diameter is the width

distribution of a 3D object in different directions. Breadth 3D is defined as the largest distance between two parallel lines touching the object without intersection it and lying in a plane orthogonal to the maximum 3D Feret diameter [See Avizo user's guide].

3. Results

3.1 Phase identification and 2D cross-sectional morphology

Figure 1 shows the X-ray diffraction spectra of the as-cast Al-5Cu-1.5Fe-1Si alloy and the equilibrium solidification phase diagram of an alloy with similar compositions [23]. The XRD (Figure 1a) shows that, in addition to the Al matrix, the alloy contains eutectic Al_2Cu, peritectic β-$Al_9Fe_2Si_2$ and ω-Al_7Cu_2Fe phases (called ω-Fe hereafter). Compared to the equilibrium phases illustrated in the phase diagram (Figure 1b), the metastable ω-Al_7Cu_2Fe appeared in the as-cast samples, not the equilibrium α-Fe (Al_8Fe_2Si). This is because the faster cooling of the sample during the casting process suppressed the peritectic transformation, i. e. $L + Al_7Cu_2Fe \rightarrow (Al) + Al_8Fe_2Si + Al_2Cu$.
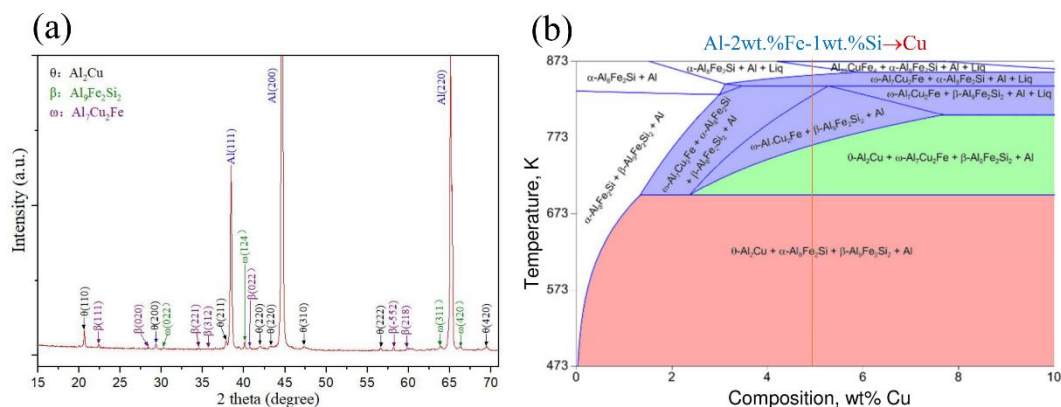
Fig. 1 (a) XRD pattern of the as-cast Al-5Cu-1.5Fe-1Si alloy; (b) vertical section of the quaternary alloy phase diagram for Al-2Fe-1Si→Cu [17]
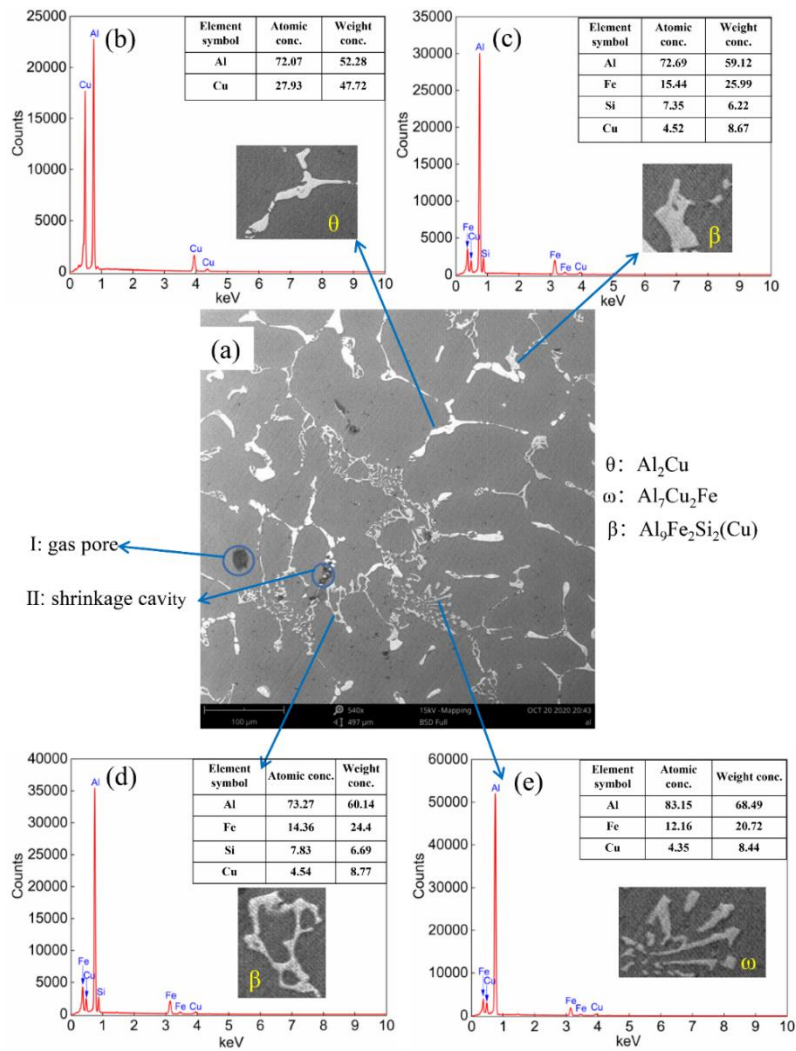
Fig. 2 Typical SEM image for the as-cast Al-5Cu-1.5Fe-1Si alloy and the corresponding EDS spectrum for the different phases; (a) A typical SEM image; (b) EDS of the Al_2Cu phase; (c) EDS of the $Al_9Fe_2Si_2(Cu)$ phase; (d) EDS of the $Al_9Fe_2Si_2(Cu)$ phase and (e) EDS of the Al_7Cu_2Fe phase

Figure 2 shows the typical SEM image of the Al-5Cu-1.5Fe-1Si alloy and the corresponding EDS spectrum for each individual phase. The Al matrix, eutectic Al_2Cu, peritectic β-$Al_9Fe_2Si_2$ phase and the black pores are clearly identified. The pores in the as-cast condition are gas pores and shrinkage cavities. The gas pores exhibit smooth and round interface (Figure 2a) while shrinkage cavities have irregular outlines in the vicinity of the Fe-rich intermetallics (Figure 2a). In the current Al-5Cu-1.5Fe-1Si alloy, the β-Fe phases form at the early stage of solidification and develop into a

complex 3D network structure [12]. They constrain the infiltration of the residual liquid at the later stage of solidification, resulting in insufficient feeding and therefore cause shrinkage cavities.

Al$_2$Cu phases are white-bright phases in the SEM image (Figure 2a). EDS reveals that their compositions are close to the stoichiometry of θ-Al$_2$Cu phase (Figure 2b). The β-Fe however exhibits different morphologies, either as polygonal blocks (Figure 2c) or Chinese script (Figure 2d). EDS shows that the β-Fe contains ~4.5%at Cu. In addition, some rod-like phases appeared at the periphery of β-Fe have contrast different to that of the β-Fe (Figure 2e), and they were identified as ω-Fe by the EDS analysis.

3.2 Phase identification by machine learning

Figure 3 shows the image processing procedure for the tomography slices. Figure 3a is a typical slice extracted from the reconstructed tomography image stack. Figure 3b shows the selected region of interest (ROI). After denoise filtering and contrast adjustment, the background noise was much reduced and the real structure features in the image became much clearer (Figure 3c), greatly facilitating the subsequent image segmentation process.

The ω-Fe phases are located at the periphery of β-Fe and their contrasts are quite similar and it is difficult for this machine learning approach to distinguish the interface between β-Fe and ω-Fe. Therefore, both β-Fe and ω-Fe are recognized as the Fe-rich phases during image processing. In the Trainable Weka Segmentation plugin of Fiji software, four classes of structural features, i. e. Al matrix, Fe-rich phase, Al$_2$Cu phase and pores were defined. Training features including Gaussian blur, hessian, membrane projections, Sobel filter, and difference of Gaussians were firstly selected

to separate the different classes by a FastRandomForest classifier. The trained classifier was then saved and applied to the whole 3D tomography image stack. The probability of pixels belonging to one specific class was mapped and the mapped 3D image stack was further segmented and refined by manually removing some noise signals in Avizo software. Figure 3d shows the typical segmented results. The segmentation by the machine learning based approach can achieve ~95% accuracy in terms of phase identification. Moreover, using machine learning approach, the time needed for processing one typical 3D image stack was reduced from 8 hours to 1 hour when compared to only use of the interactive thresholding in Avizo software.
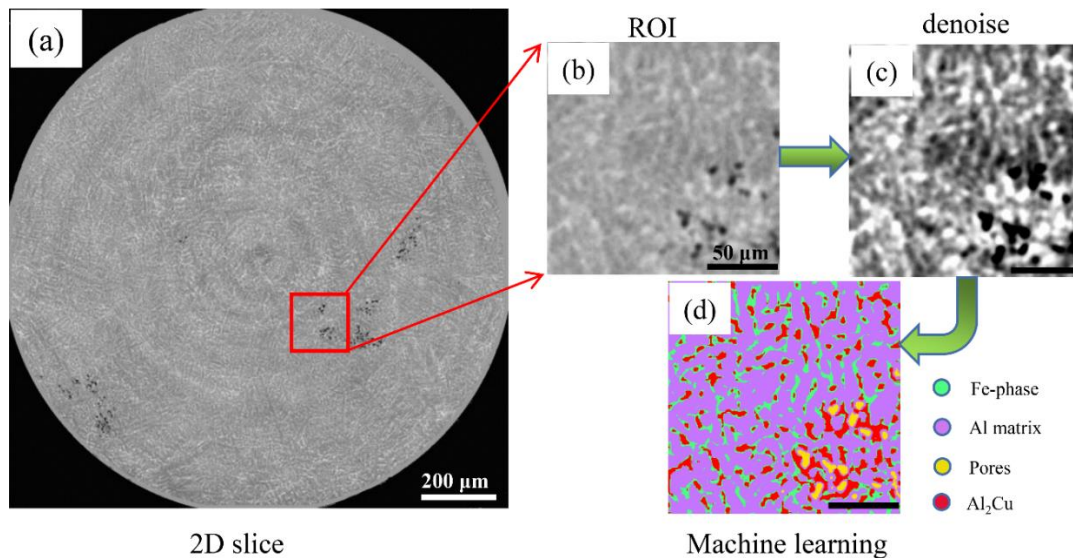

Fig. 4. A typical slice from the synchrotron X-ray tomography image stack of the as-cast Al-5Cu-1.5Fe-1Si alloy and the image processing procedure. (a) A typical 2D slice; (b) the selected region of interest (ROI); (c) the filtered and normalized image and (d) the segmented image by applying the machine learning based approach.

After segmentation, the volume fractions of each phase were calculated, and the results are shown in Table 1. The volume fraction of Al_2Cu phases in the sample is 9.3%, while the Fe-rich phases 7.9% and the pores 0.2%. Compared with the area percentages of each phase obtained from the SEM image (Figure 2a), the proportions of the Fe-rich phase and Al_2Cu phase are much higher, which is attributed to the facts

that the 2D section from SEM images do not reflect the real characteristics of the 3D structures.

**Table 1** The fractions of various phases in the as-cast Al-5Cu-1.5Fe-1Si alloy

categories	Volume fraction/%	Area fraction/%
Fe Phase	7.9	3.8
Al_2Cu Phase	9.3	2.0
Al Matrix	82.6	93.9
Pores	0.2	0.3

**3.3 3D structure and morphology of the phases and statistical analyses**

3.3.1 The Fe-rich phases

Figure 4 shows the Fe-rich phases (green) and Al_2Cu phases (red) in a selected volume of 55 x 55 x 55 μm^3. It can be seen that the majority of the Fe-rich phases and Al_2Cu phases are separated by the Al matrix. However, some of them do cross over and are entangled together in 3D space. Figure 5 shows the typical 3D morphologies of the Fe-rich phases. Figures 5a and 5b correspond to the small polygonal blocks showed in the SEM images. They are the platelet-shaped particles in 3D space. Figures 5c and 5d are the real 3D morphologies of the complex Chinese script in the SEM image. They are spatially connected network structures. Cai et al. studied the evolution of Fe-rich phase in Al-5.5Si-3.4Cu-0.87Fe-0.27Mg alloy by in situ 4D synchrotron X-ray tomography and found that the initially grown Fe-rich phase is lamellar and finally developed into a 3D network structure with lamellar dendrite arms [12]. Zhao et al. found that the Fe-phase in the solidified Al-5Cu-0.6Mn-Fe alloy demonstrates a lamellar-like 3D network structure [11]. Both morphologies are in consistency with the Fe-rich phase 3D morphology presented in this paper, suggesting

that the final solidified morphology of the Fe-rich phase are mainly affected by the morphology of the initially formed Al-Fe phases.
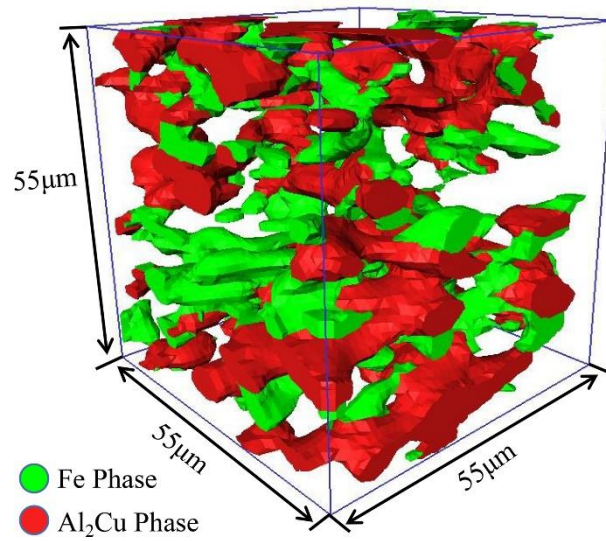
**Fig. 4** The Fe-rich phases and Al$_2$Cu phases in the selected 3D volume

Statistical analysis of the Fe-rich phases in Figure 4 indicates that the average 3D thickness of the Fe-rich phase is 6.0 μm. The minimum 3D thickness is 1.8 μm and the maximum one is 31.9 μm. The larger 3D thickness is due to the Fe-rich phase on the edge of the dendrite arms where sufficient peritectic reactions occur. Figure 5e shows the distribution of the 3D equivalent diameter of the Fe-rich phase for the whole tomography volume. The majority of the distribution is in the range of 5~8 μm. Larger 3D equivalent diameter means more complex spatially connected network structures.
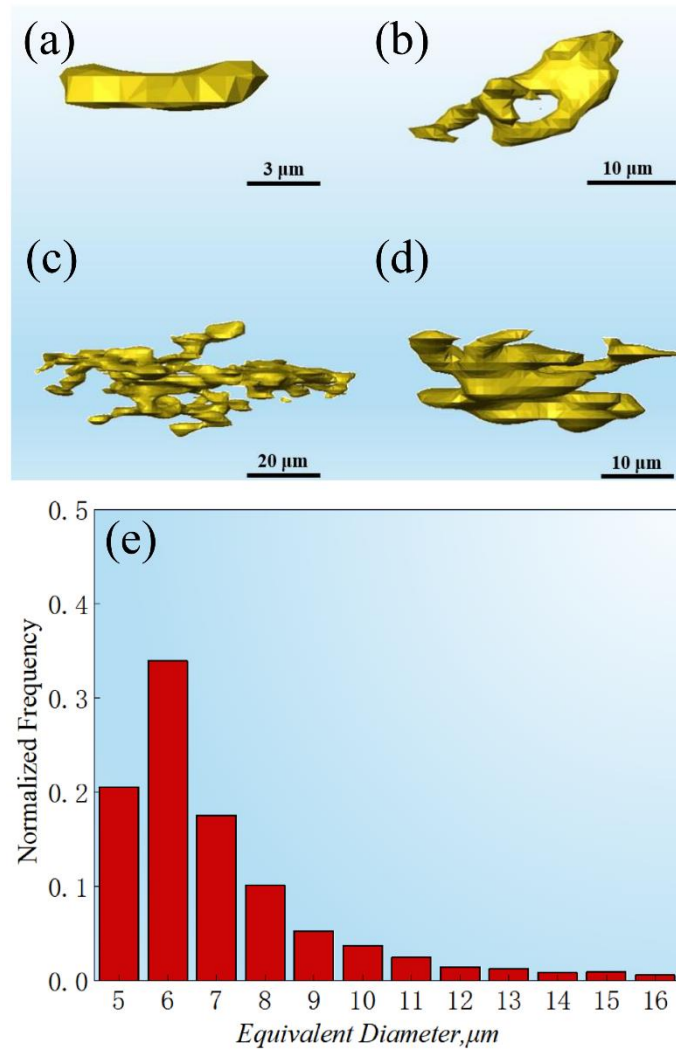
Fig. 5 The typical 3D morphologies of Fe-phase, (a) and (b) show the polygon morphology; (c) and (d) show the complex Chinese script morphology;(e) distribution of the 3D equivalent diameter of the Fe-phase

3.3.2 The Al_2Cu phases

Figure 6a and 6b shows that the 3D morphologies of the eutectic Al_2Cu phases. Most Al_2Cu phases are lathy-like particles and separated by the Al matrix. Figure 6c and 6d shows their 3D equivalent diameter and 3D thickness distribution. The 3D thickness is mainly in the range of 2~5 μm with an average 3D thickness of 3.5 μm. The 3D equivalent diameter is in the range of 5 ~ 10 μm with an average 3D equivalent diameter of 6.6 μm.
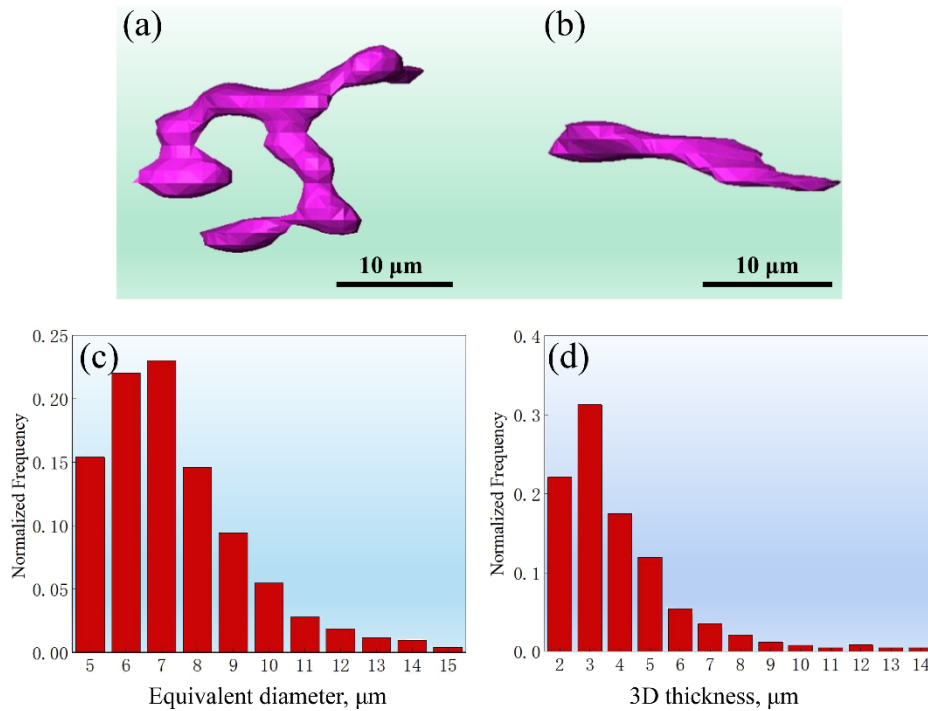
Fig. 6 (a) and (b) 3D morphologies of the eutectic Al$_2$Cu phases; (c) distribution of the equivalent diameter and (d) 3D thickness for the eutectic Al$_2$Cu phases

3.3.3 The pores and shrinkage cavities

Figure 7 shows 3D distribution of the pores in the whole sample and Figure 8a and 8b illustrates the 3D morphology of the gas pores and shrinkage cavities. The volume and roundness of the gas pore are calculated as 208 μm^3 and 0.526, respectively. In contrast, shrinkage cavities are closely linked to the formation of the Fe-rich phases at the early stage of solidification. The Fe-rich phases (including Al-Fe, Al-Fe-Si and Al-Fe-Cu phase) form before the eutectic reaction, growing into spatially connected 3D network which constrained the residual liquid feeding into the growing shrinkage and therefore created the cavities. The pores and shrinkage cavities are the origin of crack initiation and propagation [24]. Controlling and minimising the pores formed during solidification are extremely important to the quality of the cast alloys and components.

13
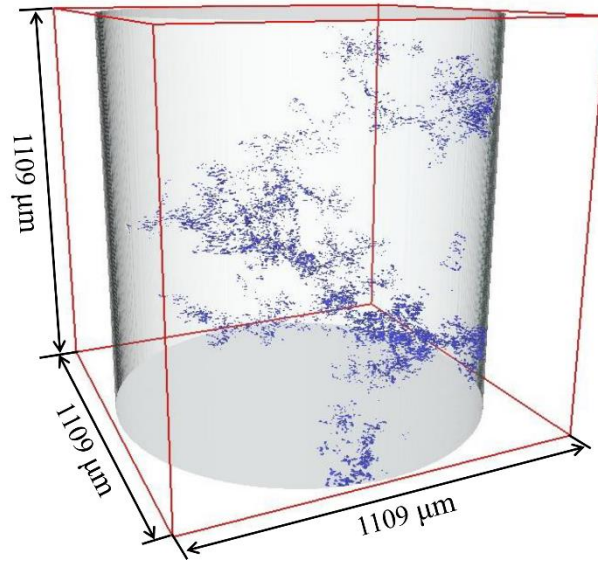
Fig. 7 3D distribution of the pores inside the sample

$$y = \frac{1}{(x-\tau)\sigma 2\pi} exp[\frac{-(ln(x-\tau)-\mu)^2}{2\sigma^2}$$

τ: 2.849
σ: 0.668
μ: 0.985
R^2: 0.9959
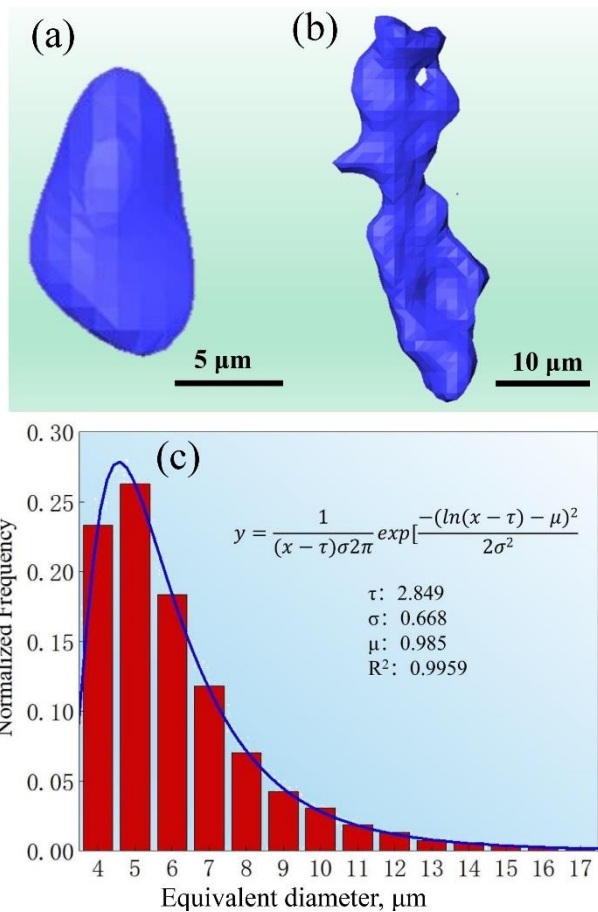
Fig. 8 3D morphologies of the pores: (a) gas pore; (b) shrinkage cavity and (c) distribution of the 3D equivalent diameter of the pores inside the sample and the fitted curve using a lognormal distribution function

Figure 8c shows that the distribution of the 3D equivalent diameter of the shrinkage cavities. The distribution follows the three-parameter lognormal probability function [25]:

$$y = \frac{1}{(x-\tau)\sigma\sqrt{2\pi}}\exp\left[\frac{-(\ln(x-\tau)-\mu)^2}{2\sigma^2}\right]$$

where τ is the threshold value [26], μ is the scale parameter; σ is the shape parameter; R^2 is the correlation fitting parameter. The calculated values of those parameters are showed in Figure 8c. The calculated threshold of 2.85 μm means that the shrinkage cavities have 3D equivalent diameter larger than 2.85 μm while $R^2 = 0.9959$ indicates that the lognormal distribution describes the shrinkage distribution very well.

4. Discussions

Most Fe-rich phases in the Al-5Cu-1.5Fe-1Si alloy exhibit complex 3D spatially connected network structure and morphologies. Similar structures were found and reported in the Al-Fe-Si alloys containing Mn [21], Mg [12] and Cu [23] elements. This indicates that the initial Al-Fe phase morphologies formed at higher temperature has significant impact on the morphology of later developed Fe-rich phases.

According to the phase diagram in Figure 1b, the Al-Fe phase is initially formed at 635 ° and grows rapidly into the liquid phase to form the skeleton network of the Al-Fe phase as the solidification starts. Al-Fe phases can form complex crystal structure depending on the stoichiometric ratios of Al versus Fe as well as the solidification conditions. Al_3Fe or $Al_{13}Fe_4$ are the common equilibrium phases in the Al-Fe binary system, which has a larger unit cell parameter (C2/m space group). In the Al-Fe-Si system, Al_3Fe is easy to form when the cooling rate is low, and the Fe/Si ratio is high

[27-28]. The crystal structure of the Al_3Fe phases also makes them easy to develop into platelet-like spatial network structures [29].

After the formation of Al_3Fe phases, primary Al dendrite begins to nucleate and grow as the temperature further decreases. However, based on the phase diagram [23], the temperature interval between the formation of Al_3Fe phase and primary Al is small (<10 °C). Al_3Fe phases can also act as nucleation sites for the primary Al, leading to a coupled and convoluted growth morphology which is often considered as the eutectic reaction between the melt and the Al_3Fe phases. When Si is present, Al-Fe-Si phase forms at the Al_3Fe surface through a peritectic transformation of L + Al_3Fe → (Al) + Al_8Fe_2Si + $A_{16}(FeCu)$ [30-31].

As temperature further decreases (at ~610°C), the peritectic reaction of L + $A_{16}(FeCu)$ →(Al) + Al_8Fe_2Si + Al_7FeCu_2 occurs. Finally, at the eutectic reaction temperature (~530°C), the final eutectic transformation: L→Al+Al_2Cu or L+Al_7Cu_2Fe→(Al) + Al_8Fe_2Si + Al_2Cu occurs [30-31].

The above phase reaction analyses indicate that the formation of both Al_8Fe_2Si phase and Al_7FeCu_2 phases are related to the peritectic reaction between liquid melt and Al_3Fe phase. Their spatial morphology inherited that of the primary Al_3Fe phase. Hence, the Fe-rich phases in Al-Fe-Si alloys often exhibit platelet-like network structure. In contrast, most of Al_2Cu phases are formed through the eutectic reaction in the residual liquid phase. Although the primary Al_3Fe phases do not participate directly the eutectic reaction to produce Al_2Cu phases, the spatial distribution of the already solidified Al_3Fe phases indeed affects the spatial distribution of Al_2Cu phases to a much extent as indicated in Figure 2 and 4. Therefore, control, alter and optimise the structure and morphology of the initially formed Al_3Fe phases are the keys to control the structures and morphologies of the different types of Fe-rich intermetallic

phases formed subsequently. Unfortunately, the Al_3Fe phases and the primary Al often grow simultaneously and coupled together in 3D space and therefore the effective way to control or alter the morphology of Fe-rich intermetallic phases is to disrupt the coupled growth. In this aspect, applying external fields into the solidification processes has demonstrated some unique advantages in breaking down the couple-growth morphologies [8-10, 29, 32].

5. Conclusions

In this work, synchrotron X-ray tomography was used to characterize the 3D morphology of the intermetallic phases in a recycled Al-5Cu-1.5Fe-1Si alloy in as cost condition. The machine learning method was adopted in phase identification, segmentation and data processing. The main findings are:

1. In the studied condition, the β-$Al_9Fe_2Si_2$ and ω-Al_7Cu_2 are the main Fe-rich intermetallic phases in the Al-5Cu-1.5Fe-1Si alloy. the β-$Al_9Fe_2Si_2$ phases exhibit a spatially connected 3D network structure and morphology which in turn control the 3D spatial distribution of the Al_2Cu phases and the shrinkage cavities. The Al_3Fe phases formed at the early stage of solidification affects to a large extent the structure and morphology of the subsequently formed Fe-rich intermetallic phases.

2. The machine learning based image processing approach is an efficient and high-fidelity phase recognition and segmentation tool for the synchrotron X-ray tomography datasets which are essential for processing big datasets in multidimensional imaging-based materials characterization work.

Acknowledgments

References

[1] J. Gronostajski, H. Marciniak, A. Matuszak. J. Mater. Process. Technol. **106 (1–3)**, 34 (2000).

[2] Guan, RG., Tie, D. Acta Metall. Sin. (Engl. Lett.) **30**, 409 (2017).

[3] Jia Li, Hongzhou Lu, Jie Guo, Zhenming Xu and Yaohe Zhou. Environ. Sci. Technol. **41(6)**, 1995 (2007)

[4] Hongzhou Lu, Zeran Hou, Mingtu Ma and Guimin Lu. Metals. **7(7)**, 262 (2017)

[5] Gaustad G, Olivetti E, Kirchain R. Resour. Conserv. Recycl. **58**, 79 (2012)

[6] Damoah, L.N.W. and Zhang, L. Metall. Mater. Trans. B **41**, 886 (2010)

[7] Mi J., In Situ Studies of the Solidification Dynamics of Metal Alloys, ed. by Eskin D., Mi J. Solidification Processing of Metallic Alloys Under External Fields, vol 273. (Springer International Publishing, 2018, ISBN 978-3-319-94842-3, DOI: 10.1007/978-3-319-94842-3)

[8] Zhiguo Zhang, Chuangnan Wang, Billy Koe, Christian M. Schlepütz, Sarah Irvine, Jiawei Mi, Acta Mater. **209**, (2021) 116796

[9] Bing Wang, Dongyue Tan, Tung Lik Lee, Jia Chuan Khong, Feng Wang, Dmitry Eskin, Thomas Connolley, Kamel Fezzaa, Jiawei Mi, Acta Mater. **144**, (2018) 505-515.

[10] Feng Wang, Dmitry Eskin, Jiawei Mi, Chuangnan Wang, Billy Koe, Andrew King, Christina Reinhard, Thomas Connolley, Acta Mater. **141**, (2017) 142-153

[11] Y. Zhao, W. Du, B. Koe, T. Connolley, S. Irvine, P.K. Allan, C.M. Schlepütz, W. Zhang, F. Wang, D.G. Eskin, J. Mi, Scripta Materialia **146** (2018) 321-326.

[12] B. Cai, A. Kao, P.D. Lee, E. Boller, H. Basevi, A.B. Phillion, A. Leonardis, K. Pericleous. Growth of β intermetallic in an Al-Cu-Si alloy during directional solidification via machine learned 4D quantification. Scripta Materialia **165**, 29 (2019).

[13] Zhiguo Zhang, Jia Chuan Khong, Billy Koe, Shifeng Luo, Shi Huang, Ling Qin, Silvia Cipiccia, Darren Batey, Andrew J. Bodey, Christoph Rau, Yu Lung Chiu, Zhu Zhang, Jean-Christophe Gebelin, Nick Green, Jiawei Mi, Scripta Materialia **193**, (2021) 71-76.

[14] Yu C L, Jiang J C. Int. J. Bioprint. **6(1)**, 253 (2020)

[15] Maceachern S J, Forkert N D. Genome. **64(4)**, 416 (2021)

[16] Zheng Xiong, Yuxin Cui, Zhonghao Liu, Yong Zhao, Ming Hu and Jianjun Hu. Comput. Mater. Sci. **171**, 109203 (2020)

[17] Pawar P J, Rao R V. Int. J. Adv. Manuf. Tech. **67(5-8)**, 995 (2013)

[18] Wang Kun, Zhang Xueliang, Zhang Suixia, Ji Xuewen and Liu Huiqiang. Chin. J. Biomed. Eng. **39(05)**, 621 (2020)

[19] Sarah Mbiki, Jerome McClendon, Angela Alexander-Bryant & Jordon Gilmore. Med. Biol. Eng. Comput. **58(7)**, 1419 (2020)

[20] Theerapatt Manuwong, Wei Zhang, Peter Lobo Kazinczi, Andrew J. Bodey, Christoph Rau & Jiawei Mi. Metall. Mater. Trans A. **46**, 2908 (2015).

[21] Yuliang Zhao, Weiwen Zhang, Billy Koe, Wenjia Du, Mengmeng Wang, Weilin Wang, Elodie Boller, Alexander Rack, Zhenzhong Sun, Da Shu, Baode Sun, Jiawei Mi. Mater. Charact. **164**, (2020) 110353

[22] T. Weitkamp, D. Haas, D. Wegrzynek and A. Rack. ANKA. J. Synchrotron Rad. **18**, 617 (2011).

[23] Basak C B, Babu N H. Sci. Rep. **7**, 1 (2017)

[24] Wan Qian, Zhao Haidong, Zou Chun. Acta. Metall. Sin. **49(03)**, 284 (2013)

[25] See D, Atwood R C, Lee P D. J. Mater. Sci. **36(14)**, 3423 (2001)

[26] Tiryakioglu M, Hudak D. J. Mater. Sci. **42(24)**, 10173 (2007)

[27] Xia Z, Wen B, Fan C Z. Metals. **9(12)**, 1322 (2019)

[28] Skjerpe P. J. Microsc. **148(1)**, 33 (1987)

[29] Lifeng Zhang, Jianwei Gao, Lucas Nana Wiredu Damoah & David G. Robertson. Mineral. Mineral Processing and Exractive Metall. Rev. **33(2)**, 99 (2012)

[30] Yu. N. Mansurov, J. U. Rakhmonov. Non-ferrous Metals. **2**, 37 (2018)

[31] Nikolay A. Belov Dmitry G. Eskin Andrey A. Aksenov. Multicomponent Phase Diagrams: Applications for Commercial Aluminum Alloys. 1st Edition 2005.

[32] Chao Fan, Si-yuan Long, Huai-de Yang, Xiang-jie Wang & Jun-cheng Zhang. Int. J. Min. Met. Mater. **20(9)**, 890 (2013)